

Supporting Information for Unique hot carrier distributions from scattering mediated absorption

Jason Codrington[†], Noor Eldabagh[†], Kimberly Fernando[†], and Jonathan J. Foley IV*

*Department of Chemistry, William Paterson University, 300 Pompton Road, Wayne, NJ,
07470, USA*

E-mail: foleyj10@wpunj.edu

*To whom correspondence should be addressed

Plots of Global Hot-Carrier Distributions

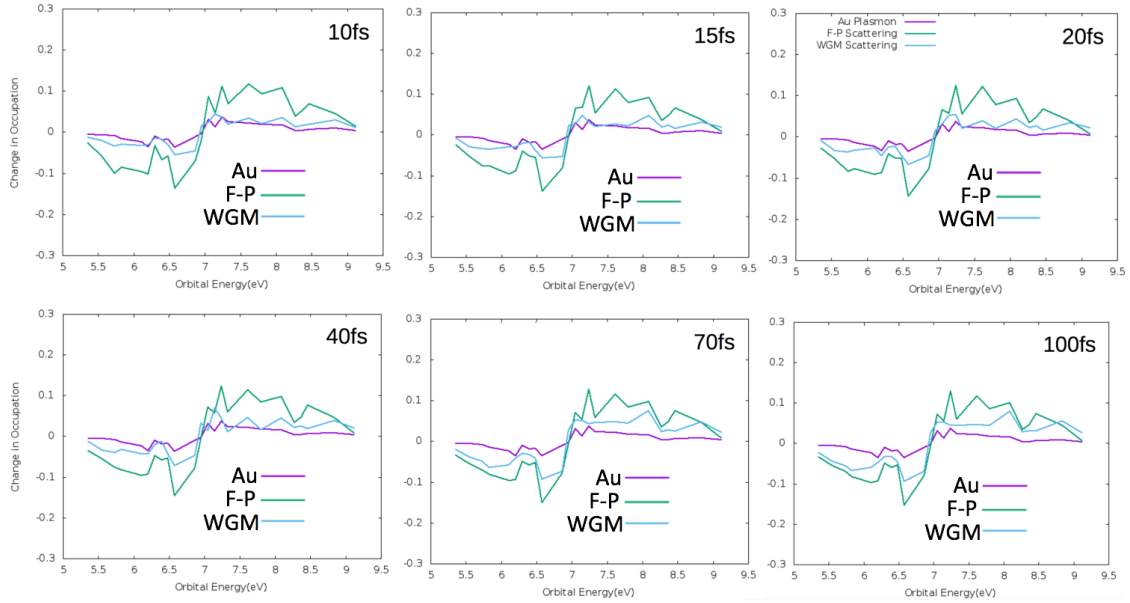


Figure S1: Snapshots of changes in occupation of each orbital in the active space of the PIW Au NC model as a measure of instantaneous hot carrier distributions. The change in orbital occupation is computed from elements of the time-dependent one-electron reduced density matrix (1 RDM) relative to their initial value, $D_p^p(t) - D_p^p(t = 0)$ for several timepoints in the simulation.

Hot-carrier dynamics in hybrid Ag/dielectric nanostructures

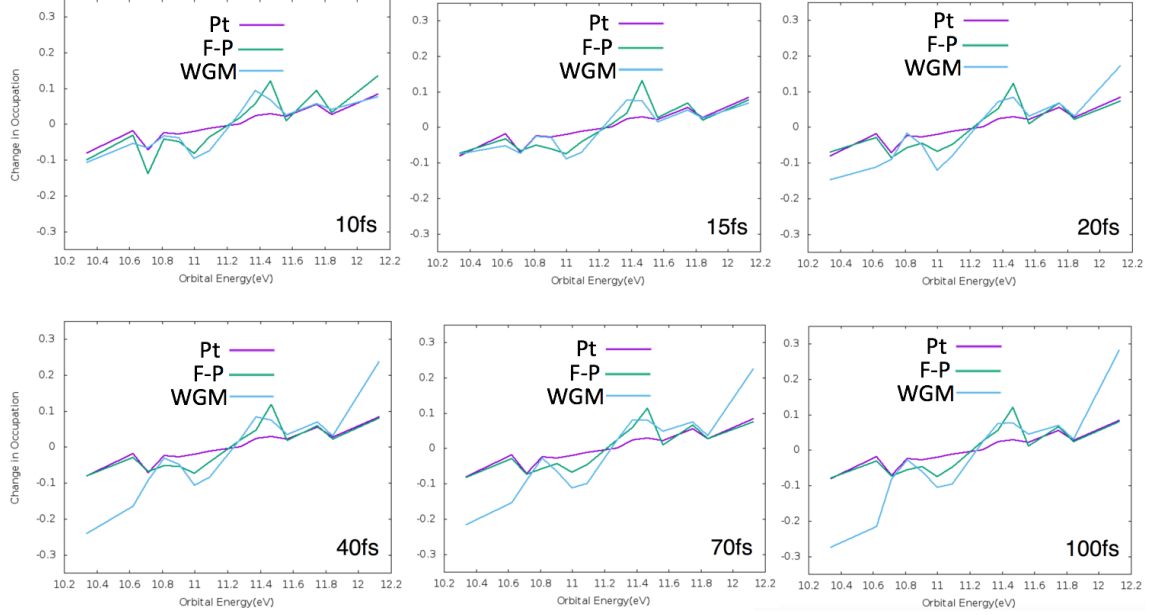


Figure S2: Snapshots of changes in occupation of each orbital in the active space of the PIW Pt NC model as a measure of instantaneous hot carrier distributions. The change in orbital occupation is computed from elements of the time-dependent one-electron reduced density matrix (${}^1\text{RDM}$) relative to their initial value, $D_p^p(t) - D_p^p(t=0)$ for several timepoints in the simulation.

Electronic structure of metal nanocubes

For cubic metal nanoparticles, we approximate the one-electron orbitals as energy eigenstates of the particle-in-a-cubic-well. For a particle confined by a cubic well with length L , the potential is 0 when $x < L, y < L, z < L$ and infinity otherwise. The energy eigenstates have the form

$$\psi_{n_x, n_y, n_z} = \left(\frac{2}{L}\right)^{3/2} \sin\left(\frac{n_x \pi x}{L}\right) \sin\left(\frac{n_y \pi y}{L}\right) \sin\left(\frac{n_z \pi z}{L}\right). \quad (1)$$

The energy eigenvalues have the form

$$\epsilon_{n_x, n_y, n_z} = \frac{\hbar^2 \pi^2}{2 m L^2} (n_x^2 + n_y^2 + n_z^2). \quad (2)$$

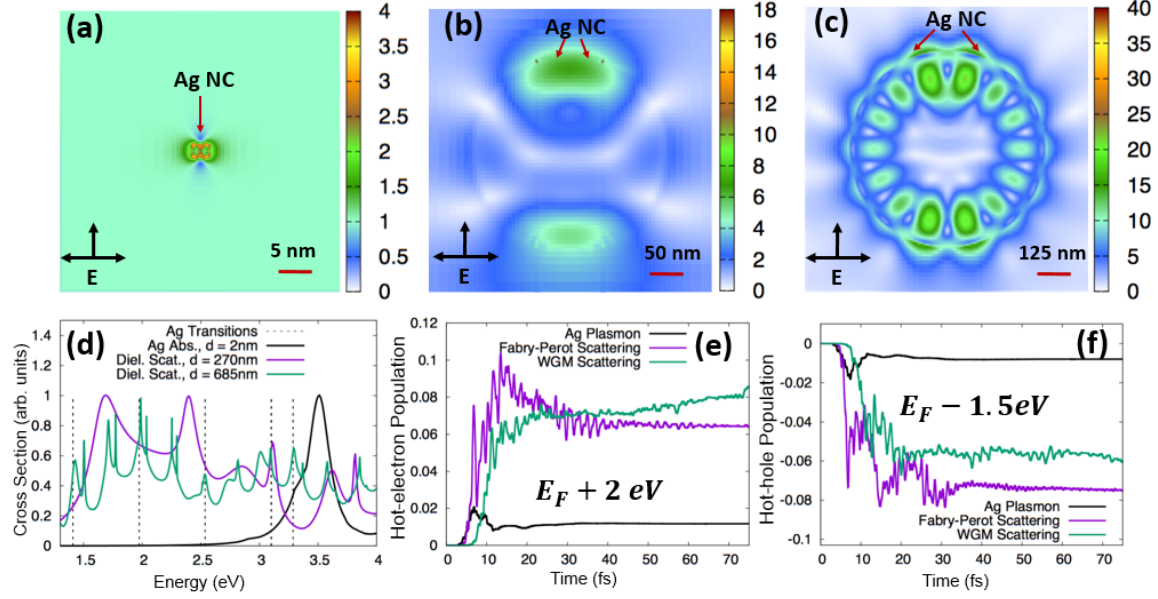


Figure S3: Three regimes for light-matter interactions leading to unique spatial and temporal shaping of the incident field, and the corresponding impact on electronic dynamics in a $L = 2\text{nm}$ PIW Ag nanocube. Plots of the near-field enhancements ($|\mathbf{E}|/|\mathbf{E}_0|$) are shown for the Ag NC LSPR ($\lambda = 400\text{nm}$, **Panel (a)**), a Fabry-Perot resonance of a $d=270\text{nm}$ dielectric nanosphere decorated with Ag NCs ($\lambda = 397\text{nm}$, **Panel (b)**), and a Whispering Gallery Mode resonance of a $d=685\text{nm}$ dielectric nanosphere decorated with Ag NCs ($\lambda = 493\text{nm}$, **Panel (c)**). The extinction spectra of these three structures are shown overlaid with the dipole-allowed transitions in the PIW model of the Ag NC, showing strong overlap between these transitions and the scattering resonances of the $d = 685\text{nm}$ dielectric nanosphere (**Panel (d)**) with only partial overlap between the Ag LSPR and dipole-allowed transitions in the PIW model. The change in orbital populations ($D_p^p(t) - D_p^p(t = 0)$) is computed to measure hot-electron and hot-hole generation. Both dielectric scattering resonances show more efficient generation of hot-electrons (**Panel (e)**) and hot-holes (**Panel(f)**) compared to LSPR in this case.

The transition dipole operator can be decomposed into its components,

$$\hat{\mu} = \hat{\mu}_x \mathbf{i} + \hat{\mu}_y \mathbf{j} + \hat{\mu}_z \mathbf{k}. \quad (3)$$

Given this model, the number of electrons for a given material can be estimated as

$$N_e = \frac{L^3}{3\pi^2} \left(\frac{2mE_F}{\hbar^2} \right)^{3/2} \quad (4)$$

where E_F is the experimental Fermi energy for the bulk material of interest. We assume close-shell systems in all cases and round to the next highest integer value of N_e . Similarly, the Fermi energy in our model can be defined as

$$E_F^{PIW} = \frac{\hbar^2}{2m} \left(3\pi^2 \frac{N_e}{L^3} \right)^{2/3}, \quad (5)$$

where E_F^{PIW} will often be slightly larger than the bulk value of the Fermi energy given that N_e in the above expression will be rounded to the next highest integer.

The transition dipole integral components can be evaluated analytically, for example, the x -component has the form

$$\begin{aligned} \langle \psi_{n_x, n_y, n_z} | \hat{\mu}_x | \psi_{n'_x, n'_y, n'_z} \rangle &= e \delta_{n_y, n'_y} \delta_{n_z, n'_z} \frac{L(\pi(n_x - n'_x)\sin(\pi(n_x - n'_x)) + \cos(\pi(n_x - n'_x)) - 1)}{\pi^2(n_x - n'_x)^2} \\ &\quad - e \delta_{n_y, n'_y} \delta_{n_z, n'_z} \frac{L(\pi(n_x + n'_x)\sin(\pi(n_x + n'_x)) + \cos(\pi(n_x + n'_x)) - 1)}{\pi^2(n_x + n'_x)^2}, \end{aligned}$$

where $\hat{\mu}_x = -ex$. Analogous expressions can be obtained for expectation values of $\hat{\mu}_y$ and $\hat{\mu}_z$.

We order the orbitals by a single index p such that $\epsilon_{p+1} \geq \epsilon_p$; that is, each ψ_{n_x, n_y, n_z} can be uniquely labeled ψ_p . Using the above expressions and following this labeling scheme, the

diagonal matrix elements can be evaluated as

$$\langle \Phi_0 | \hat{H}(t) | \Phi_0 \rangle = \sum_{p=1}^{nocc} \epsilon_p \quad (6)$$

$$\langle \Phi_i^a | \hat{H}(t) | \Phi_i^a \rangle = \sum_{p=1}^{nocc} \epsilon_p - \epsilon_i + \epsilon_a \quad (7)$$

and the off-diagonal matrix elements can be evaluated as

$$\langle \Phi_0 | \hat{H}(t) | \Phi_i^a \rangle = \mathbf{E}(t) \cdot \langle \psi_i | \hat{\mu} | \psi_a \rangle \quad (8)$$

$$\langle \Phi_i^a | \hat{H}(t) | \Phi_j^b \rangle = \mathbf{E}(t) \cdot \langle \psi_a | \hat{\mu} | \psi_b \rangle \delta_{ij} - \mathbf{E}(t) \cdot \langle \psi_i | \hat{\mu} | \psi_j \rangle \delta_{ab}. \quad (9)$$

The precise form of these matrix elements arise because of the antisymmetry of the underlying many-electron wavefunction. It is important to note that while coulomb repulsion is not included in our current approach, Pauli exclusion, which is an inherently many-body effect, is enforced by the antisymmetry of the wavefunction through the Slater-Condon rules used to derive the matrix elements in Eq. (6) through (9). Importantly, terms analogous to those in Eq. (9) are not included in methodologies like Linear Response Time-Dependent Density Functional Theory (LR-TDDFT) or methods that use time-dependent perturbation theory (TDPT) to first order. In fact, setting the terms in Eq. (9) to zero yields TDPT expressions for the rates of the CIS coefficients. The terms in Eq. (9) have an important role in the hot-carrier dynamics in SMA because of the long lifetimes associated with the scattering resonances, and hence, the long duration of the optical fields that drive these dynamics. The discrepancy between is shown in Figure S4 where we perform two calculations with the same driving field: one where the full TDCIS equations are solved, and one where the terms in Eq. (9) are set to zero, yielding a equations of motion where only transitions between the ground- and singly-excited configurations are considered, similar to linear-response or TDPT-based approaches.

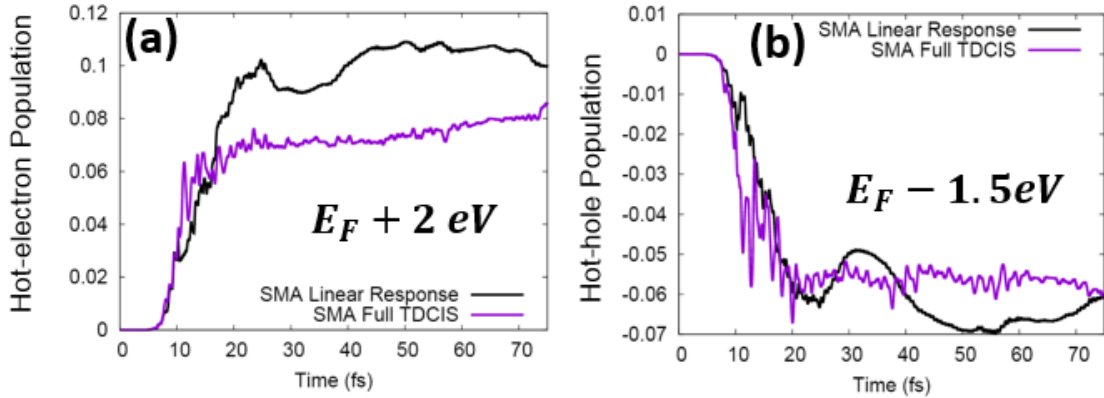


Figure S4: Comparison of hot-electron dynamics as computed from the full TDCIS method (purple line labeled SMA Full TDCIS) and one where excited-to-excited configurations are neglected in the spirit of approaches based on linear-response theory and time-dependent perturbation theory to first order (black line labeled SMA Linear Response). While the two approaches agree at short times, the long-time dynamics can show significant departure as population accumulates in excited-state configurations. These calculations consider 685 nm dielectric nanospheres ($n=2.6$) decorated with 2nm Ag nanocubes.

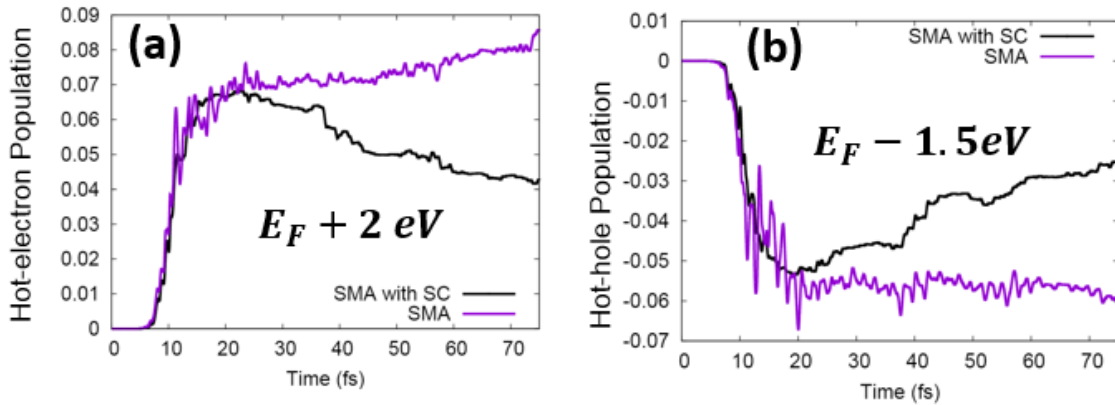


Figure S5: Comparison of hot-electron dynamics with from SMA with (black line labeled SMA with SC) and without (purple line labeled SMA) a phenomenological size correction to the dielectric function of silver in 685 dielectric nanospheres ($n=2.6$) decorated with 2 nm Ag nanocubes. The size corrections are described in Eq. (11) - (14) of this Supporting Information document.

Finite-difference time-domain calculations

A commercial simulator based on the finite-difference time-domain method¹ was used to compute the electric field, $E(t)$ 1 Å away from the nanoparticle surface in each of the scenarios considered. The displacement was taken along the z -axis, corresponding to the polarization direction of incident light since the strongest near-field enhancement is expected along this direction. A grid spacing of 1 Å in x , y , and z was utilized in a cubic region extending 1 nm beyond the metal NP surface, and a non-uniform mesh was utilized otherwise with dx , dy , $dz \leq 20nm$. For each composite structure, a nanoparticle was placed at the surface of the dielectric nanosphere at an angle of 20° with respect to the propagation axis of the incident light. In all simulations, light propagates along the x axis and is polarized along the z axis. The metal nanoparticles are centered at $y = 0$. A total-field scattered-field source was used to illuminate the structures. The FDTD simulations were terminated when the ratio of the total energy in the simulation volume to the total energy injected by the illumination source falls below 10^{-6} . Because the WGMs are higher quality factor resonances, longer time is typically required for these simulations as compared to the plasmonic particles alone.

The resulting time-domain fields were fed into our TDCIS algorithm, allowing us to simulate the electronic dynamics driven by rigorously-computed nearfields from scattering and plasmon resonances, which show strong spatiotemporal modification relative to freely propagating light. The electric field was scaled by a factor $E_0 \approx 614,000,000 V/m$ so that the peak power of the illumination source is $10^{15} W/m^2$. The electric field was sampled at intervals of approximately 2.8 attoseconds for all simulations, which leads to a time-step that ensures stability of the wavefunction propagation with the relevant energy scales of our simulations. Our TDCIS scheme requires the evaluation of the electric field at intermediate times between these timesteps, and we use a simple update based on centered-finite differences to approximate the electric fields at these times. As an example, if the electric field is known at times t_1 , $t_2 = t_1 + dt$, and $t_3 = t_1 + 2 \cdot dt$ where $dt = 2.8 as$, and knowledge of the field is required at some time $t_m = t_2 + m \cdot dt$ where m is non-integer, $E(t_m)$ is estimated as

follows:

$$\mathbf{E}(t_m) = \mathbf{E}(t_2) + \frac{\mathbf{E}(t_3) - \mathbf{E}(t_1)}{t_3 - t_1} \cdot m \cdot dt. \quad (10)$$

The optical response of Au, Pt, and Ag in the FDTD simulations utilizes permittivity data from the work of Johnson and Christy² (Au) and Palik³ (Pt and Ag). We assume a static dielectric constant of 2.6 for the dielectric nanospheres in this work, which is comparable to the visible dielectric constant of titanium dioxide. The prototype calculation of the impacts on SMA resulting from size effects in the dielectric response of silver utilizes the phenomenological size correction for the plasmon damping rate in nanocubes suggested by Coronado and Schatz,⁴

$$\gamma_{SC} = \gamma_{bulk} + \frac{Av_F}{L_{eff}} \quad (11)$$

where $L_{eff} = 2L/3$ for cubes, where L is 2 nm in this case, we take A to be 1 and v_F is taken to be 1.39×10^6 m/s for silver. We incorporate γ_{SC} into a Drude model for the intra-band contribution to silver's dielectric function,

$$\epsilon_{Drude,SC}(\omega) = 1 - \frac{\omega_P^2}{\omega^2 + i\gamma_{SC}\omega}. \quad (12)$$

We take ω_P and γ_{bulk} from a Drude+2Lorentz fit to the Palik data between 200-800 nm; specifically, $\hbar\omega_P = 8.73$ eV and $\hbar\gamma_{bulk} = 0.075$ eV. We infer the inter-band contribution to the dielectric function from the bulk experimental data and from the bulk Drude fit,

$$\epsilon_{inter}(\omega) = \epsilon_{Palik}(\omega) - \epsilon_{Drude,bulk}(\omega). \quad (13)$$

Finally, the dielectric function used for the size-corrected calculations is defined as

$$\epsilon_{SC}(\omega) = \epsilon_{inter}(\omega) + \epsilon_{Drude,SC}(\omega). \quad (14)$$

Results from these prototype calculations are shown in Figure S5.

References

- (1) Lumerical Solutions, Inc., <http://www.lumerical.com/tcad-products/mode/>.
- (2) Johnson, P. B.; Christy, R. W. Optical constants of noble metals. *Phys. Rev. B* **1972**, *6*, 4370.
- (3) Palik, E. D. *Handbook of optical constants of solids*; Academic Press, 1998.
- (4) Coronado, E. A.; Schatz, G. C. Surface plasmon broadening for arbitrary shape nanoparticles: A geometrical probability approach. *J. Chem. Phys.* **2003**, *119*, 3926.